THE JOURNAL OF PHYSICAL CHEMISTRY C

pubs.acs.org/JPCC Article

The Role of Particle Size in the Dispersion Engineering of Plasmonic Arrays

Veronika Tretnak, Ulrich Hohenester, Joachim R. Krenn,* and Andreas Hohenau

Cite This: J. Phys. Chem. C 2020, 124, 2104–2112 Read Online

ACCESS | Metrics & More | Article Recommendations | Supporting Information

ABSTRACT: Grazing diffraction orders on metal gratings give rise to peculiar optical effects that were contemplated by Wood, Rayleigh, and Fano. With plasmonic nanoparticles as resonant grating elements, the phenomenology of such surface lattice resonances becomes quite rich, including spectrally narrow extinction peaks and optical band gap formation. It has been observed that at perpendicular incidence, either the higher- or lower-energy branch corresponding to the first grazing diffraction orders is bright, that is, couples strongly to light. Reviewing the literature, it appears that particle size is the factor determining which dispersion branch lights up. However, a consistent explanation for this effect is lacking. After revisiting the effect experimentally and by numerical simulation, we clarify the underlying physics by analyzing nanoparticle gratings in terms of, first, an oscillator model and, second, a photonic crystal description. Both approaches reveal the central role of a particle size-dependent phase shift in the back-scattering of grazing light fields by the particle grating. This phase shift determines the symmetry of the resulting field profiles corresponding to the dispersion branches and thus their ability to couple to the exciting light. This physical understanding could considerably simplify the dispersion engineering of plasmonic nanoparticle gratings for specific applications as sensing or lasing.

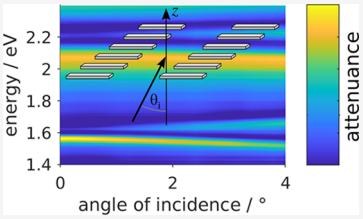

INTRODUCTION

When light is diffracted by a grating along the grating plane, anomalies in the zero-order reflection or transmission spectra appear as sudden intensity changes at defined wavelengths and incidence angles. These changes occur due to diffraction orders switching from propagating to evanescent (Rayleigh anomalies), and, in the case of metal gratings, due to the excitation of surface plasmon polaritons (Wood anomalies). For gratings built from regular arrays of metal nanoparticles, grazing diffraction orders coupling to the particle plasmon modes (local surface plasmon resonances, LSPRs) give rise to surface lattice resonances (SLRs). Depending on the mutual spectral positions of LSPRs and SLRs, the optical response of a grating can be significantly modified, resulting in spectrally narrow and energy-tunable extinction peaks.[1] These narrow line-width modes rely on the dipolar far-field coupling between particles that is in-phase with the exciting light wave, leading to strong local fields and the opening of energy gaps.[1] The appearance of SLRs in regular metal nanoparticle arrays was first theoretically described by Meier et al.[2] and Carron et al.[3] Early experimental evidence was retrieved from lithographically defined silver and gold particle arrays, however hampered by the presence of a glass/air interface that suppresses effective radiative coupling.[4−6] SLR-related effects were then shown for nanowire gratings on slab waveguides,[7,8] and SLRs were clearly demonstrated on particle arrays in a homogeneous environment.[9,10] More recent studies were looking into the role of particle and array dimensions,[11,12] the grating symmetry,[13,14] and applications as sensing[15] and lasing.[16]

When looking at the dependence of SLR frequency on the incidence angle θ_i of the exciting light, one always finds two SLR branches of the same order number that tend toward the same frequency (or photon energy) for perpendicular incidence (Figure 1). However, even for perpendicular incidence, their mutual coupling can give rise to two distinct SLR resonances due to the formation of a band gap.[17] Interestingly, experimental extinction spectra show that either the higher energy or the lower energy SLR branch looses strength upon approaching $\theta_i = 0$ where actually only one branch couples to light, that is, "bright". This is caused by the symmetry of the coupling-induced field distribution with respect to the particle center, as for perpendicular incidence only the symmetric case can couple to light. It is however unclear at this point if the symmetric field profile corresponds to the low- or high-energy SLR. Although this effect has been noticed[18−20] and analogies exist on corrugated surfaces,[17] it has been rarely addressed and no comprehensive interpretation in physical terms has been given to the best of our knowledge. However, the reported data suggest that particle size plays a central role. Indeed, particles with a length l (measured perpendicular to the polarization of incident light) exceeding half the grating pitch d are observed to give rise to a bright high-energy SLR branch at $\theta_i = 0$. This includes, for example,

Received: November 4, 2019
Revised: December 24, 2019
Published: December 24, 2019

https://dx.doi.org/10.1021/acs.jpcc.9b10235
J. Phys. Chem. C 2020, 124, 2104–2112

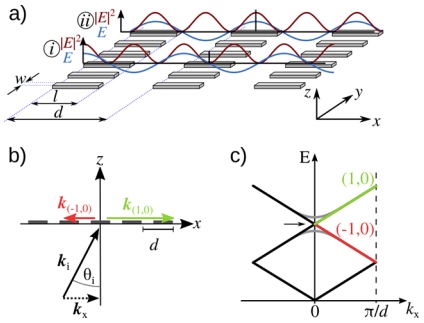

Figure 1. (a) Sketch of a grating formed by a nanoparticle array in homogeneous environment with pitch d, l is the particle length in x direction, w is the particle width. (i) and (ii) show the intensity profile (red) and a momentary snapshot of the electric field (E) distribution (blue) of the standing waves formed by the (±1,0) diffraction orders that fulfill the translational and mirror symmetries of the array. (b) Illumination geometry in the x−z plane: $k_x = 2\pi/\lambda$, $k_x = k_x \sin \theta_i$, and θ_i is the incidence angle. (c) Sketch of the empty lattice dispersion of grazing diffraction orders, i.e., energy E vs k_x. When coupling of the (±1,0) diffracted waves is taken into account, a band gap opens at $k_x = 0$ (gray lines, arrow).

gold nanorods with a long axis around 420 nm, arranged in a regular array with d = 600 nm.[11,21,22] Conversely, particles with $l < d/2$ show a bright low-energy branch at perpendicular light incidence, as observed, for example, for gold nanodisks with a diameter of 120 nm arranged in an array with d = 500 nm[12] and further gold and silver nanoparticle arrays.[12,16,18,23]

Here, we aim at a clear physical understanding of these intriguing characteristics in SLR light coupling of a regular nanoparticle array in a symmetric environment. We first discuss general aspects and experimental observations and inspect the effect by the coupled dipole approximation and numerical simulation. We then employ an oscillator model and a 1D photonic crystal description as simple intuitive physical models to extract the underlying physical effects. We choose this approach rather than focusing on just one model, as the different viewpoints allow us to elaborate the effects from different perspectives. Depending on further questions to be addressed, one model might furthermore prove more effective and convenient than the other.

We consider a regular 2D square array of nanoparticles (pitch d, width w, and length l) in a homogeneous environment of refractive index n (Figure 1a). A light field with wave vector $\mathbf{k}_i$ and wavelength $\lambda = \lambda_0/n$ is incident under an angle θ_i in the x−z plane (Figure 1b). The incident s-polarized (i.e., parallel to y) light wave polarizes the particles in the y direction, and their dipolar scattering being thus preferentially emitted to directions in the x−z plane. The first grazing diffraction orders in the x−z plane occur for $\lambda = d(1 \pm \sin \theta_i)$, with the plus sign for diffraction orders in the $+x$ or (+1,0) direction and the minus sign for diffraction orders in the $-x$ or (−1,0) direction. This is conveniently visualized by the empty lattice dispersion of diffracted light propagating parallel to the substrate, that is, photon energy E vs. k_x, folded into the first Brillouin zone (Figure 1c). When including coupling between the (±1,0) diffraction orders,[11,24] energy repulsion and anticrossing arise at the crossing points of the empty lattice dispersion (arrow in Figure 1c), giving rise to the opening of a band gap and thus two separate SLRs at perpendicular incidence. However, fundamental symmetry considerations suggest that at perpendicular incidence, only one SLR branch can couple to light.

At $\theta_i = 0$, the system of the particle array and incoming light is mirror-symmetric with respect to a y−z plane through the particle center, thus both diffraction orders are identical in amplitude and phase. The intensity profile of the interference pattern formed by the superposition of the (+1,0) and (−1,0) waves has to adhere to this mirror symmetry as well as the translational symmetry of the array. Thus, only two options exist, with either an intensity minimum or a maximum above the particle centers, sketched as (i) and (ii) in Figure 1a, corresponding to the two SLR branches. When considering the field instead of intensity, it is evident that only the standing wave with an intensity maximum at the particle center fulfills the symmetry requirement. However, this does not clarify whether this SLR corresponds to the low- or the high-energy branch. To address this question, in the following, we first revisit the effect experimentally and by numerical simulation, before moving on to the oscillator and photonic crystal models. We focus on square arrays of aluminum nanorods with the long axis l oriented along x (Figure 1a). As the polarization of the incident light is in the y direction, that is, parallel to the short rod axis, the correspondingly excited LSPR is basically independent of the nanorod length. We further assume that the short-axis LSPR is spectrally well separated from the (±1,0) SLRs, situated at their high-energy side.

EXPERIMENT

We start by illustrating the bright versus dark SLR branch effect around normal incidence with experimentally recorded optical attenuance spectra from square nanorod arrays (d =

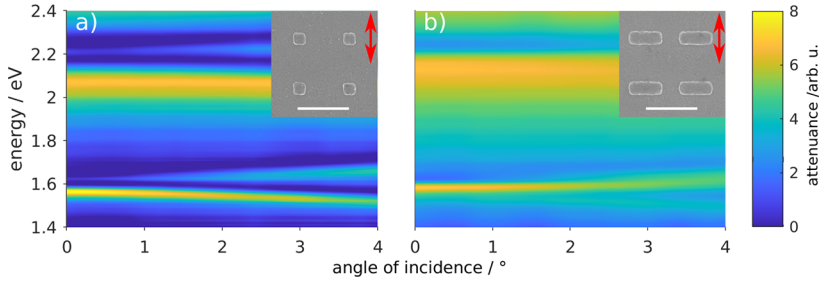

Figure 2. Measured attenuance (color scale) vs. angle of incidence and photon energy of square arrays (d = 500 nm) of aluminum nanorods of 110 nm width, 30 nm height, and lengths of (a) 120 nm and (b) 320 nm. The arrays rest on a 80 nm-thick ITO layer on glass and are immersed in oil with a refractive index of 1.516. The (±1,0) SLRs are close to 1.6 eV. The LSPR and the (±1,±1) SLRs give rise to the features around 2.1 and 2.2 eV. The insets show SEM images of the arrays (scale bar: 500 nm), and the illumination polarization direction is marked with the red double arrows.

https://dx.doi.org/10.1021/acs.jpcc.9b10235
J. Phys. Chem. C 2020, 124, 2104−2112

500 nm) fabricated on indium tin oxide (ITO, 80 nm thickness)-covered glass by standard electron beam lithography (Figure 2). The rods have a width of w = 110 nm, a height of 30 nm, and lengths of (a) l = 120 nm and (b) l = 320 nm. The attenuance spectra were recorded by a microspectrometer equipped with a microscope objective with a numerical aperture (NA) of 0.075 (half opening angle about 4°) and a condensor with an NA of 0.028 (half opening angle about 1.6°). The samples were immersed in index matching oil with a refractive index of 1.516. In Figure 2, the (±1,0) orders show up around 1.6 eV. For perpendicular incidence (Θ_i = 0°), we observe only one prominent SLR peak for both arrays of long and short nanorods. This peak shifts to lower energies for the short nanorods when increasing the incidence angle, that is, it corresponds to the (−1,0) SLR branch (Figure 2a). Conversely, the peak shifts to higher energies for the long nanorods, thus corresponding to the (+1,0) SLR branch (Figure 2b). In both cases, the SLR branch that is dark at perpendicular incidence gains strength for increasing angles of incidence. Around an incidence angle of 4°, both SLR branches show comparable signals. The further features in Figure 2 correspond to the LSPR peak at about 2.1 eV and the (±1,±1) SLRs around 2.2 eV. We note that due to the finite optical apertures in our spectrometer, the signals are averaged over some angular range. While in this case, care has to be taken in the interpretation of band gaps in the observed data,[8] our discussions and conclusions in the following are not concerned by this point (also compare Supporting Information SI1).

DISCUSSION

Coupled Dipole Approximation. A simple but successful approach to model SLRs is the coupled dipole approximation,[9] giving results (Figure 3a) that are in excellent agreement with the measurements of short nanorods (Figure 2a). The scattering of the metal nanoparticles forming the array is therein approximated by that of point dipoles. The dipoles are driven by the superposition of the incoming wave and the scattered waves from all other point dipoles representing the particles in the array. Thus, the induced particle dipole moment differs from that of an isolated particle and is expressed as an effective polarizability

$$\alpha_e = \frac{1}{1/\alpha - S}$$

where α is the the quasi-static polarizability of a particle[9] and

$$S = \sum_{a,b} e^{-(r_{ab}/\sigma)^2} e^{ikx_a \sin(\theta_i)} e^{ikr_{ab}} \left[\frac{k^2 \sin^2 \varphi}{r_{ab}} \right]$$

is the retarded dipole sum. The center coordinate of a particle/dipole with indices a and b (Figure 3b) is $\mathbf{r}_{ab} = (a, b)d$, $r_{ab} = |\mathbf{r}_{ab}|$, $x_a = ad$, and φ = arctan (a/b). The exciting light is polarized in the y direction and incident under an angle θ_i. In extension to the usually used expression,[9] here S includes a Gaussian term $e^{-(r_{ab}/\sigma)^2}$ to account for the limited interaction length and finite spatial coherence of the incoming light. According to the approximate spatial coherence of the illumination optics, σ was set to 20 μm and the sum defining S was extended over a range of 5σ in x and y directions. We only consider the dipolar far-field term, as we observed no obvious changes by including the near field term for the relevant array parameters.

With the dielectric function of Al from ref 25 and fitted to the experimental case (Figure 2a) in terms of the nanorod shape factor (to mach the LSPR) and volume (to mach the band splitting), the calculated angle-dependent attenuance is depicted in Figure 3a. There is excellent qualitative agreement with the experimental data, and in particular, only the low-energy, (−1,0) SLR is bright for small incidence angles. In addition, band gap formation as well as the (±1,±1) SLRs and the LSPR at higher energy fits well to the experiment, thus confirming the observation on the small nanorod arrays. Note that we had to assume particle volumes of only 1/14 of the actual values. The coupled dipole approximation fails when applied to the real nanorod volumes, yielding nonphysical results since the radiation losses of the point dipoles are not properly considered by the quasi-static polarizability.

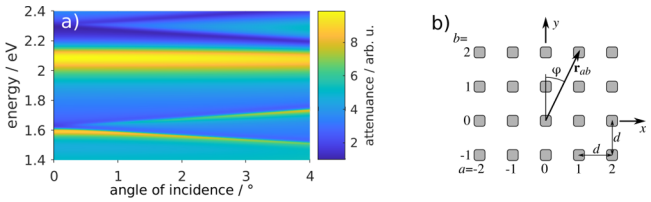

Figure 3. (a, b) Calculated attenuance (color scale) vs. angle of incidence and photon energy in the coupled dipole approximation, for a square array of particles as sketched in (b) with d = 500 nm. $\mathbf{r}_{ab}$ is the distance vector from the origin to the particles center with row and column indices a and b. The particles are approximated by point dipoles located at the particle center with a polarizability fitted to match the experimental spectra. For perpendicular incidence, only the low-energy SLR couples significantly to light.

Numerical Simulations. To fully address the nanorod size range of interest, we turn to numerical simulations with the MNPBEM toolbox[26] that relies on the boundary element method, supplemented with periodicity. We compare aluminum nanorods of 100 and 300 nm lengths that are 100 nm

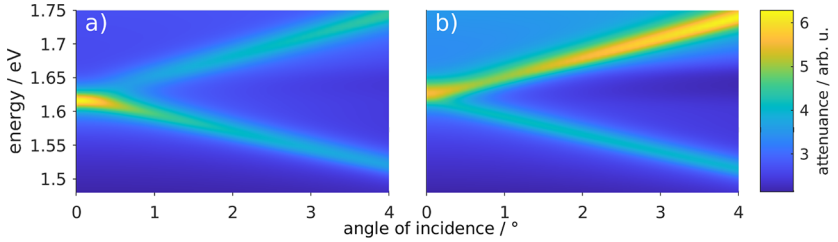

Figure 4. MNPBEM simulated attenuance (color scale) vs. angle of incidence and photon energy for arrays (d = 500 nm) of aluminum nanorods of 100 nm width, 300 nm height, and lengths of (a) 100 nm and (b) 300 nm in homogeneous environment of refractive index 1.516. The energy of the bright SLR branch obviously depends on the nanorod length.

https://dx.doi.org/10.1021/acs.jpcc.9b10235
J. Phys. Chem. C 2020, 124, 2104−2112

wide and 300 nm high, arranged in a square array (d = 500 nm) in a homogeneous medium of a refractive index of 1.516. The dielectric function for aluminum was taken from ref 25. While there are some deviations as compared to the experimental sample for practical reasons, these lead to only minor spectral changes with no impact on the conclusions with regard to the SLR characteristics. The simulated attenuance is plotted in Figure 4 in a color scale versus energy and angle of incidence, focusing on the (±1,0) SLR spectral range. From the plots, the two dispersion branches are evident, as is the bright character of the low-energy branch at perpendicular incidence for the shorter nanorod (Figure 4a), while for the longer nanorod, the high-energy branch lights up (Figure 4b).

It could be assumed that further insight regarding the discussed phenomenon can be inferred from the nanorod polarization patterns, as multipolar LSPRs appear at different energies and they differ in their light coupling efficiencies in dependence on their specific polarization symmetries. However, this is hardly the case as the nanorod polarization is off-resonant and mainly reflects the local electric field strength that is a superposition of the incident light field and the diffracted (±1,0) orders. To illustrate this point, we depict in Figure 5

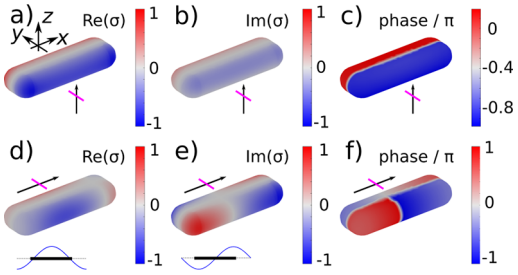

Figure 5. Simulated normalized surface charge density σ (color scale) of a 300 nm-long aluminum nanorod (width 100 nm and height 30 nm). Excitation with a y-polarized plane wave at 1.6 eV, propagating in (a–c) $+z$ direction and in (d–f) $+x$ direction. σ is plotted for the moment in time when the maximum of the exciting electric field is at (a, d) the particle center (Re(σ)) and (b, e) a quarter period later (Im(σ)). (c) and (f) The corresponding phase patterns. The bottom insets depict the electric field strength (blue) of the exciting wave along the nanorod (black) in the x direction.

the polarization charge density of a 300 nm-long aluminum nanorod (width 100 nm and height 300 nm), excited by simple fields only, that is, with a single, y-polarized plane wave at 1.6 eV (i.e., close to the SLR energy), propagating in the $+z$ or $+x$ direction. In Figure 5a–c, the exciting wave is propagating in the $+z$ direction and the polarization charge density is basically independent of the x coordinate. It follows the off-resonant (i.e., in-phase) polarization induced by the exciting field, with only little phase lag. In Figure 5d–f, the exciting wave is propagating in the $+x$ direction and, depending on the moment of time, we either find a (d) dipolar or (e) quadrupolar charge density pattern. Importantly, these are momentary snapshots of a polarization wave propagating along x and must not be confused with the mode pattern of resonantly excited dipolar or quadrupolar LSPRs that appear at much higher energies for the parameters chosen here. The nanorod geometry induces just a barely visible higher charge density at the rod edges, and there is no prominent phase shift or mode-specific charge pattern as to be expected for resonant LSPR excitation. With respect to the symmetry aspect that governs the coupling of the resulting standing field pattern to light,[11] we have to conclude that the consideration of LSPR mode patterns does not contribute to solve our problem.

Oscillator Model. We now turn to an approach as sugested, for example, in ref 11, where the SLRs and the LSPR are qualitatively described as coupled oscillators with resonance frequencies and coupling and damping constants as fitted to the measured spectra. In the following, by some approximations, we connect this model to the physics of our nanoparticle arrays and thereby focus on the (±1,0) SLRs.

When neglecting the near fields of the individual particles, the electromagnetic field in the grating plane is the sum of of the incident wave and the two waves propagating parallel to the grating plane in the (±1,0) directions. Assuming that in the y direction, the rods can be approximated as a wire-like structure, only the field along the major axis varies over the nanorods, and the problem under consideration becomes one-dimensional. The field then can be written in the form

$$\mathbf{E}(x) = (e^{ik_x x}E_i + e^{ikx}E_+ + e^{-ikx}E_-)\hat{\mathrm{y}}$$

where E_i and $E_\pm$ are the complex-valued amplitudes of the incident (i) and the (±1,0) waves, $k_x = k_i \sin\theta_i$ is the parallel component of the wave vector of the wave incident at angle θ_i, and $k = nk_0$ is the wavenumber of the waves propagating in the (±1,0) directions.

From the simulations discussed above, we find that the rods are polarized under nonresonant conditions such that the dipole moment per unit length $\mathbf{p}(x)$ of the polarization charges is proportional to the electric field $\mathbf{E}(x)$ according to

$$\mathbf{p}(x) = \alpha(x)\mathbf{E}(x) = \alpha(x)(e^{ik_x x}E_i + e^{ikx}E_+ + e^{-ikx}E_-)\hat{\mathrm{y}}$$

with $\alpha(x)$ being the polarizability per unit length. We can now take the reversed viewpoint and treat the dipole density as the source for the scattered electromagnetic fields. We express the scattered field produced by the dipole density $\mathbf{p}(x')$ of the rods through[27]

$$\mathbf{E}_s(x) = e^{ikx}\mathbf{E}_+ + e^{-ikx}\mathbf{E}_- = \mu_0\omega^2 \sum_a \int_{-l/2}^{l/2} G_{yy}(x, x_a + x')\mathbf{p}(x_a + x')\,\mathrm{d}x'$$

where G is the dyadic Green tensor describing the field at x due to a column (along y) of nanorod segments at $x_a + x'$ polarized with dipole density $\mathbf{p}$. The index a (compare Figure 3b) labels the columns (along y) of rods in the array, which have a length l and are centered at x_a. In what follows, we assume that the right-moving wave with an amplitude $\mathbf{E}_+$ is produced by two independent sources, namely, through scattering of the incident wave into the (+1,0) direction and through back-scattering of the $\mathbf{E}_-$ wave from (−1,0) to (+1,0). The scattered fields can be approximated as outgoing waves $e^{ik(x - x' - x_a)}$ modulated by some distance-dependent factor to account for out-of-plane scattering, finite interaction length, and spatial coherence. We lump the distance dependence into effective coupling parameters g_i^+ (coupling of incident to the (+1,0) wave) and g_b (back-scattering of (−1,0) to (+1,0) wave), to arrive at

https://dx.doi.org/10.1021/acs.jpcc.9b10235
J. Phys. Chem. C 2020, 124, 2104–2112

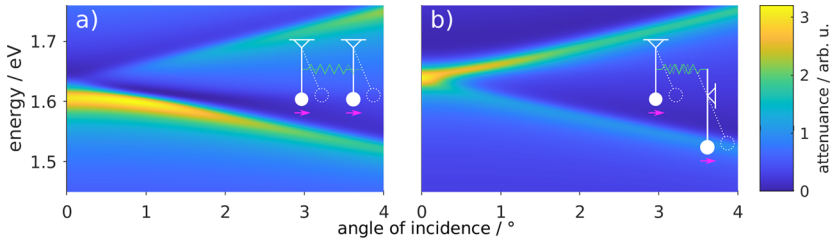

Figure 6. Calculated attenuance (color scale) vs. angle of incidence and photon energy in the oscillator model of arrays (d = 500 nm) of nanorods with (a) l = 100 nm (low-energy branch is bright at normal incidence) and (b) l = 300 nm (the high-energy branch is bright at normal incidence). A homogeneous environment with a refractive index of 1.156 was assumed. The insets sketch the mechanical coupled pendulum model to visualize the effect of the phase change in coupling between the grazing diffraction orders. For symmetric excitation (purple arrows), the low-energy mode is excited in (a), but the high-energy mode is excited in (b).

$$e^{ikx}E_+ \approx \sum_a{}' \int_{-l/2}^{l/2} e^{ik(x-x'-x_a)}[g_i^+(x_a)e^{ik_x(x_a+x')}E_i + g_b(x_a)e^{-ik(x_a+x')}E_-]\,\mathrm{d}x' \tag{1}$$

The prime on the sum indicates that we only have to sum over rods with center positions $x_a < x$, since the sources of the right-moving waves must be located to the left of x. Equation 1 has two terms, one proportional to E_i and the other proportional to E_-. For the factor of E_i, we get

$$\left(\sum_a{}' e^{-i(k-k_x)x_a}g_i^+(x_a)\right)\left(\int_{-l/2}^{l/2} e^{-i(k-k_x)x'}\,\mathrm{d}x'\right) = \frac{2}{k-k_x}S_i^+(k)\sin\left(\frac{kl}{2}\right) \tag{2}$$

where S_i^+ is a lattice sum that only depends on the lattice positions x_a, similarly to our previous expression for point dipoles, and $\sin(kl/2)$ is a form factor that only depends on the length l of the rods. Similarly, for the back-scattering, we get

$$\left(\sum_a{}' e^{-2ikx_a}g_b(x_a)\right)\left(\int_{-l/2}^{l/2} e^{-i2kx'}\,\mathrm{d}x'\right) = \frac{1}{k}S_b(k)\sin(kl) \tag{3}$$

with the lattice sum $S_b(k)$ and the form factor $\sin(kl)$. Importantly, the form factor in eq 2 is positive for $l < \frac{\lambda}{2}$ and becomes negative for $l > \frac{\lambda}{2}$. As we will discuss in a moment, this sign change causes the switch of the intensity maximum from the lower to the upper SLR branch.

From eq 1, we get

$$\begin{aligned} E_+ &= \left[\frac{2}{k-k_x}S_i^+(k)\sin(kl/2)\right]E_i + \left[\frac{1}{k}S_b(k)\sin(kl)\right]E_- \\ E_- &= \left[\frac{2}{k-k_x}S_i^-(k)\sin(kl/2)\right]E_i + \left[\frac{1}{k}S_b(k)\sin(kl)\right]E_+ \end{aligned} \tag{4}$$

where the expression for E_- in the second line has been derived along the same lines as the expression for E_+.

The lattice sums S are functions that show pronounced maxima at frequencies or k, where the exponent in the summands of eqs 2 and 3 is a multiple of 2π, for example, $(k - k_x)x_a = m2\pi$. They can be approximated by Lorentzians centered at $k_\pm = nK/(n \pm \sin\theta_i)$ and $k_b = K = 2\pi/d$.

$$S_i^+(k) = \frac{A_i}{k_-^2 - k^2 - i\Gamma_- k}$$

$$S_i(k) = \frac{A_i}{k_+^2 - k^2 - i\Gamma_+ k}$$

$$S_b(k) = \frac{A_b}{k_b^2 - k^2 - i\Gamma_b k}$$

With this, eq 4 turns into a set of equations describing two coupled, driven oscillators, however with a frequency-dependent, asymmetric stimulus.

The results of the oscillator model are depicted in Figure 6. We plot $|E^i + E^+ + E^-|^2$ for (a) l = 100 nm and (b) l = 300 nm, with $k = nk_0$ (n = 1.516). The polarizability per unit length is as well approximated as a classical, driven oscillator model, $\alpha_d = 1/(\omega_{\mathrm{LSPR}}^2 - \omega^2 - i\Gamma_{\mathrm{LSPR}}\omega)$ with Γ_{LSPR} = 0.4 eV and ω_{LSPR} = 2.1 eV. We find good qualitative agreement with the experiments as well as the numerical simulations, foremost the change of brightness from the low-energy to the high-energy SLR branch when going from short to long nanorods.

At inclined incidence (more than 1°), the maxima of S_i^+ and S_i^- are at different k or energies that are far from the maximum of S_b, thus the coupling term of eq 4 is close to zero and the equations reduce to two uncoupled equations for E_+ and E_-

$$\begin{aligned} E_+ &\simeq \frac{2}{k-k_x}S_i^+(k)\sin(kl/2)E_i \\ E_- &\simeq \frac{2}{k+k_x}S_i^-(k)\sin(kl/2)E_i \end{aligned}$$

Depending on k, either the E_+ or the E_- wave is dominantly excited.

In contrast, at perpendicular incidence ($\sin(\theta_i) = 0$), $k_+ = k_- = k_b = K$. When assuming equal lattice sums $S_i^- = S_i^+ = S_b$, the equations are simplified to

$$\begin{aligned} E_+ &= \frac{1}{k}S_b[2\sin(kl/2)E_i + \sin(kl)E_-] \\ E_- &= \frac{1}{k}S_b[2\sin(kl/2)E_i + \sin(kl)E_+] \end{aligned}$$

which are equivalent to a set of equations describing two symmetrically driven, coupled, classical oscillators. Under the given symmetric excitation, only symmetric modes with amplitude

$$E_+ = E_- = E_i\frac{(2A_b/k)\sin(kl/2)}{k_b^2 - k^2 - i\Gamma_b k - (A_b/k)\sin(kl)} \tag{5}$$

https://dx.doi.org/10.1021/acs.jpcc.9b10235
J. Phys. Chem. C 2020, 124, 2104−2112

can be excited, whereas the antisymmetric mode with $E_+ = -E_-$ remains dark.

Importantly, within this model, we find a physical interpretation for the SLR brightness in the phase change of the nanorod length-dependent form factor for the back-scattering $\sin(kl)$. If the SLR condition at normal incidence $k = 2\pi/d$ is fulfilled, $\sin(kl)$ changes the sign at $l = d/2$ and thus the phase of interaction between $(-1,0)$ and $(+1,0)$ wave turns by π. If $l < d/2$, then $\sin(kl) > 0$, thus k_b^2 that defines the resonance position in eq 5 is reduced by (A_b/k) sin (kl), shifting the resonance to lower energies as compared to the uncoupled system. If $l > d/2$, then $\sin(kl) < 0$ and the resonance is shifted to higher energies.

We try to visualize this in a mechanical model with a set of coupled pendula (Figure 6, insets). For the system sketched in Figure 6a, the symmetric oscillation mode is the low frequency mode, and as for a symmetric movement of the masses, no interaction force is exerted by the spring. The (not excitable) antisymmetric oscillation mode causes a compression and extension of the spring with additional back-driving forces, thus increasing the frequency. For the system sketched in Figure 6b, the coupling is inverted. Here, the excitable mode with symmetric movement of the masses leads to a compression or extension of the coupling spring, thus causing an additional back-driving force, shifting this mode to higher frequencies than the antisymmetric mode, where no interaction force is exerted. This finally corroborates and explains with an intuitive model the particle length-dependent light coupling of the SLR branches.

1D Photonic Crystal Model. When placing a nanoparticle array on a slab waveguide (e.g., a 80 nm-thick ITO layer as in the experiment above) for increased coherent interaction and considering $(\pm1,0)$ SLRs only, the system resembles a 1D photonic crystal (PC), a description that we discuss in the following. For sufficiently small distances between the nanorods and y polarization (so that the nanorods mainly diffract light into waveguide modes propagating in the x direction), we can interpret the nanorod rows (along y) as domains of higher refractive index n_a, while the space between the rows corresponds to regions of lower refractive index n_b (compare Figure 7).

The dispersion relation of a PC can be calculated by finding the eigenvalues of the transfer matrix M of the PC.[12] The fields E_N in the N^{th} unit cell are related to those in the $N-1^{\text{st}}$ unit cell by

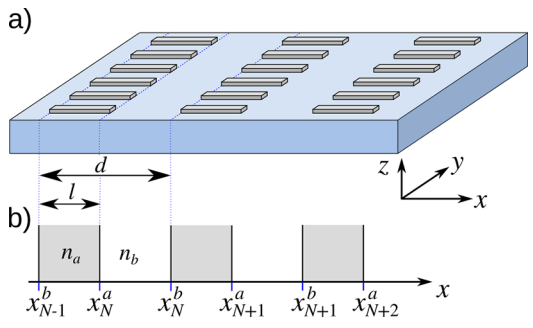

Figure 7. (a) Modeling a regular array (period d) of nanorods (length l) on a slab waveguide as a 1D PC by considering $(\pm1,0)$ SLRs only. (b) The areas occupied by the particles are described by a high refractive index n_a, while the space in between is assigned a low refractive index n_b.

$$(E_N^+, E_N^-) = M(E_{N-1}^+, E_{N-1}^-)$$

and have to obey the periodicity d of the 1D PC due to its translational symmetry. Thus,

$$(E_N^+, E_N^-) = M(E_{N-1}^+, E_{N-1}^-) = \beta(E_{N-1}^+, E_{N-1}^-)$$

with $\beta = e^{ikd}$ being the eigenvalues of M from which the wavenumber k of the eigenmode can be calculated as a function of frequency (for details see Supporting Information SI2).

To adopt this model to the current problem of particle array extinction, we need to introduce an excitation term. Therefore, we assume that a light wave is excited in the $\pm x$ directions at every interface of the 1D stack in a phase with a driving wave (E_0) incident at an angle θ_i to the interfaces. Formally, one can write this as

$$M(E_N^+, E_N^-) = \beta(E_N^+, E_N^-) + (E_S^+, E_S^-)$$

(where $E_S^{\pm}$ is not the excitation amplitudes but functions thereof, see the Supporting Information SI1) and then calculate the amplitudes of the left- and right-propagating waves as

$$(E_N^+, E_N^-) = (M - \mathbb{1}\beta)^{-1}(E_S^+, E_S^-)$$

From this, we get the amplitudes of the $(+1,0)$ and $(-1,0)$ diffracted waves and can estimate the attenuance of the 1D PC by assuming its proportionality to $|E_N^+ + E_N^- + E_0|^2$.

The results of this calculation are plotted in Figure 8. Again, we find a qualitatively similar behavior to the experiments and numerical simulations, showing a dependence of branch brightness on the length of the high refractive index zone, that is, the particle length. At perpendicular incidence, the bright branch is the high-energy one for long particles and the low-energy one for smaller particles. Consistent with the oscillator model, a closer analysis reveals that upon increasing the length of the high index areas to $l > d/2$, the coupling between E_N^+ and E_N^- changes its phase by π. We illustrate this by calculating the reflection of a layer system as discussed above, assigning $n_a = 1.516 \times (1.05 + 0.008i)$ to nanorod regions and $n_b = 1.516 \times (1.01 + 0.005i)$ to the space in between. We approximated the reflectivity from a semi-infinite PC by that of a finite one and chose 100 bilayers as a value safely assuring convergence. In Figure 9, we plot the reflection coefficient in terms of amplitude (ρ) and phase (ϕ) in dependence of energy. We observe again a phase shift of π between the reflection phase of small particles ($l = 0.2d$, Figure 9a) and large particles ($l = 0.8d$, Figure 9b). This phase shift changes the symmetry of the standing wave over the nanorod array and is thus the underlying cause for the change in SLR branch brightness. Moreover, the amplitude and phase in Figure 9 resemble closely those of a damped harmonic oscillator around resonance, however, with an additional phase lag linear in k and the π phase shift for longer particles. This connects the 1D PC model firmly to the oscillator model discussed before.

For a closer look on the transition in SLR branch brightness, we simulate the array attenuance for a continuously changing nanorod length while keeping all other parameters constant (d = 500 nm, w = 100 nm, and rod height = 30 nm). In Figure 10, we plot the attenuance for an incidence angle of 0.5°, resulting from (a) MNPBM simulations and (b) PC model calculations. At short rod length, the attenuance is following the low-energy SLR branch. With increasing rod length, this peak shifts to higher energies due to the decrease of the back-scattering

https://dx.doi.org/10.1021/acs.jpcc.9b10235
J. Phys. Chem. C 2020, 124, 2104−2112

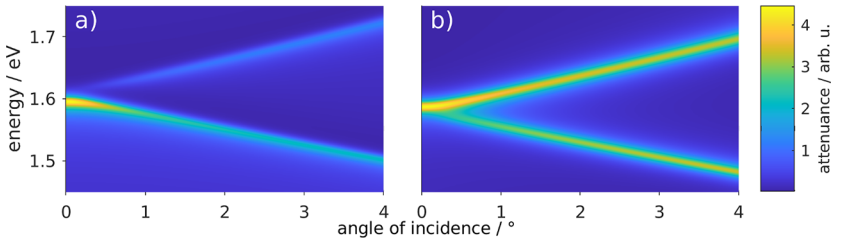

Figure 8. Calculated attenuance (color scale) of a driven, 1D PC in dependence of angle of incidence and energy for (a) l = 100 nm and (b) l = 300 nm. The refractive indices are 1.516 × (1.05 + 0.008i) for the high index region and 1.516 × (1.01 + 0.005i) for the low index region, d = 500 nm. Both a change in SLR branch brightness between both cases and a band gap at perpendicular incidence are observed.

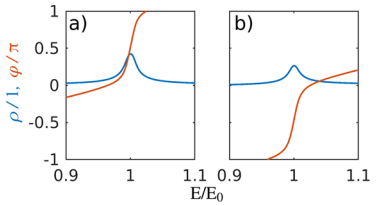

Figure 9. Reflection amplitude ρ (blue) and phase φ (orange) of 100 bilayers of n_a = 1.516 × (1.05 + 0.008i) and n_b = 1.516 × (1.01 + 0.005i) with (a) l = 100 nm and (b) l = 300 nm, d = 500 nm. Around the resonance condition at energy E_0 that corresponds to the appearance of the grazing grating order at perpendicular incidence, the reflection amplitude and phase resemble a damped harmonic oscillator. The phase is defined relative to the center of region a.

efficiency of the nanorods with increasing length, as illustrated by the oscillator model discussed above. Consequently, the coupling between forward and backward scattered SLR is reduced, evident from the reduction in band splitting. Around l = d/2, the bright mode changes from the low-energy to the high-energy SLR mode (due to the phase shift in back-scattering) and then again shifts to higher energies for further increasing values of l as back-scattering efficiency and thus the band splitting increases again. These effects are clearly reproduced by both approaches, MNPBEM simulations (Figure 10a) and the PC model (Figure 10b), with only little model-specific differences. For example, in the MNPBEM simulation, the change in brightness appears slightly below l = d/2, which is related to the small but finite phase shift between exciting wave and particle polarization (compare Figure 5). We note that a figure similar to those in Figure 10 is plotted in a publication of Rodriguez et al.,[18] in the context of far-field-induced transparency of nanorod arrays.

Energy Argument. Describing a regular particle array as a PC suggests to consider the field energies of the associated PC modes. We thus ask for the field energies in the 1D PC model, that is, a dielectric multilayer stack with alternating layers of refractive indices n_i. Due to basic symmetry considerations, within the layer stack, only two standing wave solutions due to the superposition of the (±1,0) SLRs can exist, which correspond to symmetric and antisymmetric field profiles with respect to the layer centers, as already discussed above for particle arrays (Figure 1a). Generally, these profiles have different ratios of their fields in the high and low index regions, as depicted in Figure 11. This is important as, on the one hand,

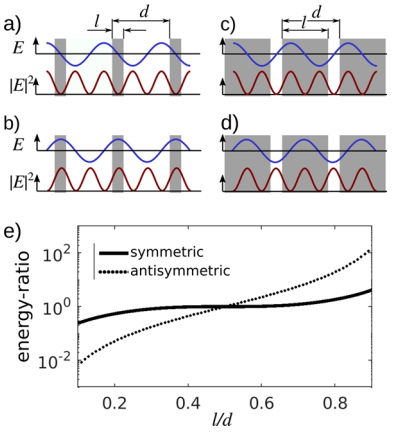

Figure 11. Sketches of the field (blue) and intensity (red) profiles of the antisymmetric and symmetric standing light fields for (a, b) small and (c, d) large particles, respectively, with l particle length and d grating pitch. (e) Particle length-dependent ratio of field energy in the high and low index regions for the symmetric (solid) and antisymmetric (dotted) standing wave patterns.

a field profile with a larger share in the high index regions corresponds to a low-frequency mode. On the other hand, a higher share in the low index regions leads to a high-frequency mode.[28] Depending on the index contrast, the two solutions are separated by an energy gap. For the sake of simplicity, we presume that the index contrast is low and neglect the

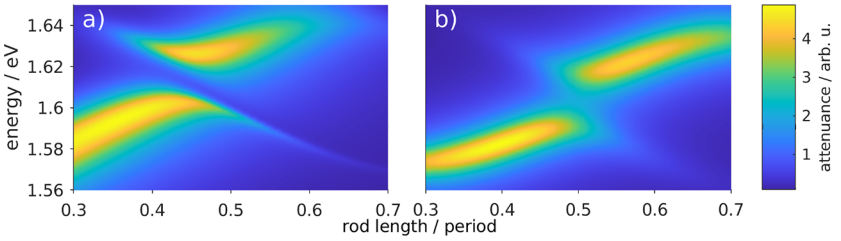

Figure 10. Attenuance spectra simulated with (a) MNPBEM and (b) the PC model in dependence of the nanorod length for 0.5° incidence angle. For the MNPBEM simulation, w × h × l = 80 × 30 × l nm^3, d = 500 nm. For the PC model, we chose as well a period of 500 nm and refractive indices of 1.516 × (1.05 + 0.008i) for the nanorod region and 1.516 × (1.01 + 0.005i) for the region in between.

https://dx.doi.org/10.1021/acs.jpcc.9b10235
J. Phys. Chem. C 2020, 124, 2104−2112

corresponding change in wavelength (see Supporting Information SI3). Including these effects does not change the qualitative nature of the effect.[28]

Applying this approach to the nanorod system, Figure 11a sketches the antisymmetric case for $l = 0.2d$. The field energy (proportional to $|E|^2$, red line) in the high index (dark) region is low as $|E|^2$ has a minimum there. Accordingly, we find this to be the high frequency mode. Evidently, due to symmetry, this mode cannot be excited at normal incidence. The optically excitable, symmetric mode, as sketched in Figure 11b, has a larger fraction of the field in the high index region and thus corresponds to the low frequency mode, in accordance with the experiment. The situation is opposite for $l = 0.8d$. For the antisymmetric case (Figure 11c), the field energy in the low index region is rather low as the field has a node there, that is, the larger part of the field energy is situated in the high index region. This field profile corresponds thus to the low frequency mode, which again due to symmetry does not couple to light at perpendicular incidence. On the other hand, the symmetric mode (Figure 11d) has a larger fraction of its field in the low index region and accordingly represents the mode at high frequency. It thus becomes clear that the symmetric modes that can couple to light at normal incidence (and close to it) are found at low energy for small particles ($l < d/2$) but a high energy for large particles ($l > d/2$). This is also evident from the ratio of the energies in the respective regions, as plotted in Figure 11e.

The lower energy mode is the one, which has more energy in the high index region relative to the other one. At $l/d < 0.5$, the ratio of energy in the high index region of the (excitable) symmetric mode (solid line) is above that of the antisymmetric mode (dotted line) and thus, the symmetric mode is the low-energy mode, whereas at $l/d > 0.5$, the situation is reversed.

CONCLUSIONS

While the array geometry sets the dispersion relation of regular plasmonic nanoparticle gratings, it is the particle size (in relation to the grating pitch) that determines if the low- or high-energy SLR branch couples to light. Both the oscillator and the PC model reveal that the physical reason for this effect is a phase shift of the light back-scattered from the particles upon interaction with grazing grating modes, occurring when the particle length equals half the grating pitch. As the relevant observable, attenuance data calculated with the models agree excellently with the experiments and numerical simulations.

Our results are not restricted to arrays of rod-shaped metal nanoparticles as dealt with in this paper. As long as the SLRs are sufficiently strong, the same effects can be observed for nonmetallic materials (see Supporting Information SI4). For other particle geometries than nanorods, the basic behavior remains the same. The crossover point of the phase change in back-scattered light, however, which is responsible for the change in brightness, will not appear at exactly $d = l/2$ but at other dimensions, depending on the particle scattering diagram and phase. Understanding the underlying physical effect in the light coupling characteristics of regular plasmonic nanoparticle gratings could largely benefit the design of such structures, for example, in view of applications in sensing[15] and lasing.[16]

ASSOCIATED CONTENT

Supporting Information

The Supporting Information is available free of charge at https://pubs.acs.org/doi/10.1021/acs.jpcc.9b10235.

Additional measurements of the SLR dispersion, the derivation of the photonic crystal model, and notes on the approximation of the field energy and on the extension to nonmetallic particles (PDF)

AUTHOR INFORMATION

Corresponding Author

Joachim R. Krenn − *University of Graz, Graz, Austria*; Email: joachim.krenn@uni-graz.at

Other Authors

Veronika Tretnak − *University of Graz, Graz, Austria*

Ulrich Hohenester − *University of Graz, Graz, Austria*

Andreas Hohenau − *University of Graz, Graz, Austria*; orcid.org/0000-0002-9034-3044

Complete contact information is available at: https://pubs.acs.org/10.1021/acs.jpcc.9b10235

Notes

The authors declare no competing financial interest.

ACKNOWLEDGMENTS

The authors thank the Austrian Research Promotion Agency (FFG) and the Austrian Climate and Energy Funds for funding this work under the project PlasmOLED (841148).

REFERENCES

(1) Kravets, V. G.; Kabashin, A. V.; Barnes, W. L.; Grigorenko, A. N. Plasmonic Surface Lattice Resonances: A Review of Properties and Applications. *Chem. Rev.* **2018**, *118*, 5912−5951.

(2) Meier, M.; Liao, P. F.; Wokaun, A. Enhanced Fields on Rough Surfaces − Dipolar Interactions Among Particles of Sizes Exceeding the Rayleigh Limit. *J. Opt. Soc. Am. B* **1985**, *2*, 931−949.

(3) Carron, K. T.; Lehmann, H. W.; Fluhr, W.; Meier, M.; Wokaun, A. Resonances of Two-Dimensional Particle Gratings in Surface-Enhanced Raman-Scattering. *J. Opt. Soc. Am B* **1986**, *3*, 430−440.

(4) Lamprecht, B.; Schider, G.; Lechner, R. T.; Ditlbacher, H.; Krenn, J. R.; Leitner, A.; Aussenegg, F. R. Metal Nanoparticle Gratings: Inuence of Dipolar Particle Interaction on the Plasmon Resonance. *Phys. Rev. Lett.* **2000**, *84*, 4721−4724.

(5) Haynes, C. L.; McFarland, A. D.; Zhao, L.; Van Duyne, R. P.; Schatz, G. C.; Gunnarsson, L.; Prikulis, J.; Kasemo, B.; Käll, M. Nanoparticle Optics: The Importance of Radiative Dipole Coupling in Two-Dimensional Nanoparticle Arrays. *J. Phys. Chem. B* **2003**, *107*, 7337−7342.

(6) Félidj, N.; Laurent, G.; Aubard, J.; Lévi, G.; Hohenau, A.; Krenn, J. R.; Aussenegg, F. R. Grating-Induced Plasmon Mode in Gold Nanoparticle Arrays. *J. Chem. Phys.* **2005**, *123*, 221103.

(7) Linden, S.; Kuhl, J.; Giessen, H. Controlling the Interaction between Light and Gold Nanoparticles: Selective Suppression of Extinction. *Phys. Rev. Lett.* **2001**, *86*, 4688−4691.

(8) Christ, A.; Tikhodeev, S. G.; Gippius, N. A.; Kuhl, J.; Giessen, H. Waveguide-Plasmon Polaritons: Strong Coupling of Photonic and Electronic Resonances in a Metallic Photonic Crystal Slab. *Phys. Rev. Lett.* **2003**, *91*, 183901.

(9) Auguié, B.; Barnes, W. L. Collective Resonances in Gold Nanoparticle Arrays. *Phys. Rev. Lett.* **2008**, *101*, 143902.

(10) Kravets, V. G.; Schedin, F.; Grigorenko, A. N. Extremely Narrow Plasmon Resonances Based on Diffraction Coupling of Localized Plasmons in Arrays of Metallic Nanoparticles. *Phys. Rev. Lett.* **2008**, *101*, No. 087403.

(11) Rodriguez, S. R. K.; Abass, A.; Maes, B.; Janssen, O. T. A.; Vecchi, G.; Gómez Rivas, J. Coupling Bright and Dark Plasmonic Lattice Resonances. *Phys. Rev. X* **2011**, *1*, No. 021019.

(12) Rodriguez, S. R. K.; Schaafsma, M. C.; Berrier, A.; Gómez Rivas, J. Collective Resonances in Plasmonic Crystals: Size Matters. *Phys. B* **2012**, *407*, 4081−4085.
(13) Humphrey, A. D.; Barnes, W. L. Plasmonic Surface Lattice Resonances on Arrays of Different Lattice Symmetry. *Phys. Rev. B* **2014**, *90*, No. 075404.
(14) Guo, R.; Hakala, T. K.; Törmä, P. Geometry Dependence of Surface Lattice Resonances in Plasmonic Nanoparticle Arrays. *Phys. Rev. B* **2017**, *95*, 155423.
(15) Thackray, B. D.; Kravets, V. G.; Schedin, F.; Auton, G.; Thomas, P. A.; Grigorenko, A. N. Narrow Collective Plasmon Resonances in Nanostructure Arrays Observed at Normal Light Incidence for Simplied Sensing in Asymmetric Air and Water Environments. *ACS Photonics* **2014**, *1*, 1116−1126.
(16) Hakala, T. K.; Rekola, H. T.; Väkeväinen, A. I.; Martikainen, J. P.; Nečada, M.; Moilanen, A. J.; Törmä, P. Lasing in Dark and Bright Modes of a Finite-Sized Plasmonic Lattice. *Nat. Commun.* **2017**, *8*, 13687.
(17) Barnes, W. L.; Preist, T. W.; Kitson, S. C.; Sambles, J. R. Physical Origin of Photonic Energy Gaps in the Propagation of Surface Plasmons on Gratings. *Phys. Rev. B* **1996**, *54*, 6227−6244.
(18) Rodriguez, S. R. K.; Janssen, O. T. A.; Lozano, G.; Omari, A.; Hens, Z.; Rivas, J. G. Near-Field Resonance at Far-Field-Induced Transparency in Diffractive Arrays of Plasmonic Nanorods. *Opt. Lett.* **2013**, *38*, 1238−1240.
(19) Shi, L.; Hakala, T. K.; Rekola, H. T.; Martikainen, J.-P.; Moerland, R. J.; Törmä, P. Spatial Coherence Properties of Organic Molecules Coupled to Plasmonic Surface Lattice Resonances in the Weak and Strong Coupling Regimes. *Phys. Rev. Lett.* **2014**, *112*, 153002.
(20) Moerland, R. J.; Hakala, T. K.; Martikainen, J.-P.; Rekola, H. T.; Väkeväinen, A. I.; Törmä, P. Strong Coupling Between Organic Molecules and Plasmonic Nanostructures. In *Quantum Plasmonics*; Bozhevolnyi, S. I., Martin-Moreno, L., GarciaVidal, F., Eds.; Springer International Publishing: Cham, Switzerland, 2017; Vol. *185*, pp 121−150.
(21) Abass, A.; Rodriguez, S. R.-K.; Gómez Rivas, J.; Maes, B. Tailoring Dispersion and Eigen-field Profiles of Plasmonic Surface Lattice Resonances. *ACS Photonics* **2014**, *1*, 61−68.
(22) Vecchi, G.; Giannini, V.; Gómez Rivas, J. Surface Modes in Plasmonic Crystals Induced by Diffractive Coupling of Nanoantennas. *Phys. Rev. B* **2009**, *80*, 201401.
(23) Zakharko, Y.; Held, M.; Graf, A.; Rödlmeier, T.; Eckstein, R.; Hernandez-Sosa, G.; Hähnlein, B.; Pezoldt, J.; Zaumseil, J. Surface Lattice Resonances for Enhanced and Directional Electroluminescence at High Current Densities. *ACS Photonics* **2016**, 3, 2225−2230.
(24) Väkeväinen, A. I.; Moerland, R. J.; Rekola, H. T.; Eskelinen, A.-P.; Martikainen, J.-P.; Kim, D.-H.; Törmä, P. Plasmonic Surface Lattice Resonances at the Strong Coupling Regime. *Nano Lett.* **2014**, *14*, 1721−1727.
(25) McPeak, K. M.; Jayanti, S. V.; Kress, S. J. P.; Meyer, S.; Iotti, S.; Rossinelli, A.; Norris, D. J. Plasmonic Films Can easily be Better: Rules and Recipes. *ACS Photonics* **2015**, *2*, 326−333.
(26) Hohenester, U.; Trügler, A. MNPBEM - A Matlab Toolbox for the Simulation of Plasmonic Nanoparticles. *Comput. Phys. Commun.* **2012**, *183*, 370−381.
(27) Novotny, L.; Hecht, B. *Principles of Nano-Optics*, 2nd ed.; Cambridge University Press: Cambridge, U.K., 2012.
(28) Joannopoulos, J. D.; Johnson, S. G.; Winn, J. N.; Meade, R. D. *Moulding the Flow of Light*; Princeton University Press: Princeton, N.J., 2008.

https://dx.doi.org/10.1021/acs.jpcc.9b10235
J. Phys. Chem. C 2020, 124, 2104−2112